

UNOBSERVED OBJECT DETECTION USING GENERATIVE MODELS

Subhansu S. Bhattacharjee^{*†}, Dylan Campbell^{*}, Rahul Shome^{*}

^{*}School of Computing, The Australian National University

Abstract

Can we detect an object that is *not* visible in an image? This study introduces the novel task of 2D and 3D unobserved object detection for predicting the location of objects that are occluded or lie outside the image frame. We adapt several state-of-the-art pre-trained generative models to solve this task, including 2D and 3D diffusion models and vision–language models, and show that they can be used to infer the presence of objects that are not directly observed. To benchmark this task, we propose a suite of metrics that captures different aspects of performance. Our empirical evaluations on indoor scenes from the RealEstate10k dataset with COCO object categories demonstrate results that motivate the use of generative models for the unobserved object detection task. The current work presents a promising step towards compelling applications like visual search and probabilistic planning that can leverage object detection beyond what can be directly observed.

1 Introduction

Object detection is a fundamental building block of perceptual systems that are capable of making sense of their surroundings. However, it is limited to visible surfaces inside the camera’s field-of-view. While amodal object detection and segmentation [68, 28] relaxes this requirement to allow partially-visible objects, we would like to go further and consider those objects that were not observed at all. One might expect this to be possible, since humans are highly capable of extrapolating the likely position of unseen objects given a context view. However, this functionality has not yet emerged for machine vision. In this paper, we propose the novel task of unobserved object detection in 2D and 3D for inferring the presence of objects unseen in an input image within a domain that extends *beyond* the camera frustum and behind the visible surfaces. We are particularly motivated by probabilistic planning tasks, where a robot might be expected to use its understanding of a scene beyond what it can directly see to undertake a reasonable action. For example, consider the setup in Figure 1. A robot tasked with locating a seated person might find it useful to look to the right, where it is likely that additional chairs would be found, or to move to view a potentially occluded chair. Predicted

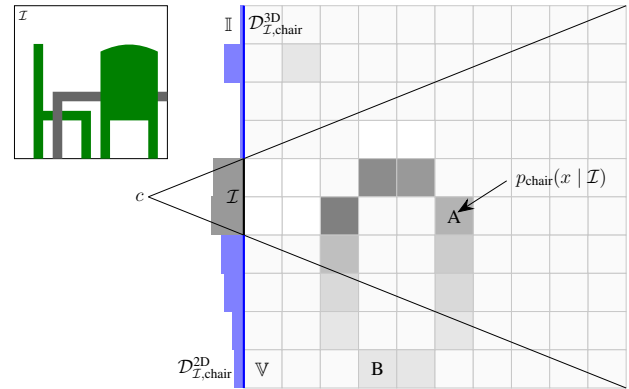


Figure 1: Unobserved object detection aims to infer the location of objects that were not directly observed in an image. Consider this toy example of a dining table and chairs. Here we visualize a top-down view (slice) of the predicted discrete distributions $\mathcal{D}_{\mathcal{I}o}^{2D}$ and $\mathcal{D}_{\mathcal{I}o}^{3D}$ for the object label o of “chair”, conditioned on the image \mathcal{I} , where darker is more probable. The presence of an occluded chair (A) is predicted as relatively likely, as is the presence of an out-of-frame chair (B). Crucially, the domain \mathbb{V} of the predicted 3D distribution exceeds the bounds of the camera frustum (drawn in black) and the domain \mathbb{I} of the 2D distribution extends beyond the image plane \mathcal{I} .

[†]Corresponding author. Contact: subhansu.bhattacharjee@anu.edu.au

spatial likelihoods of objects in the scene can inform probabilistic models [23, 35] that take decisions based on this information.

We expect a wide category of other downstream tasks, including active vision, navigation and visual search [1, 48, 64], to be enabled by solutions to this task. In these contexts, a broader understanding of the scene from learned priors can prove critical. Sampling plausible scenes conditioned on an input image correspond to a category of closely related problems where generative models have shown promising performance. While explicitly embedding spatio-semantic representations into training processes can be challenging [58], such relationships might be variationally inferred [22] using generative models trained on large-scale 2D image datasets. Novel view synthesis and semantic scene completion [57, 55, 10, 7, 46, 53] or scene-graph representations [26] can offer useful spatio-semantic priors that can be used to render 3D volumes where the object might exist. However, occlusions and incomplete or sparse data still pose significant challenges to 3D scene generation methods. Image diffusion models [18, 54] have been shown to be useful at expanding beyond the visible frame, known as outpainting [39], and some 3D diffusion models [55] can generate 3D representations consistent with an input image. However, these approaches aim for photorealism of a completed scene, which may not be necessary or desirable for unobserved object detection, where we want to infer a spatio-semantic distribution of possible scenes.

This study formally defines the unobserved object detection task in 2D and 3D, given a single image as input, and proposes three novel detection pipelines for the task. The latter extends three major categories of generative model (2D and 3D diffusion models and vision–language models) to address this task. We also propose metrics to evaluate the performance of the detection pipelines at unobserved object detection, which measure the diversity and accuracy of the predictions. In summary, our contributions are:

1. defining the novel task of unobserved object detection;
2. extending three major classes of generative model to address the task of unobserved object detection; and
3. benchmarking these methods on a suite of metrics designed for this unobserved object detection.

We evaluated the methods on the RealEstate10k dataset [67] using MS-COCO object labels [27] in 2D, 2.5D and 3D task settings. The results indicate that existing pre-trained models exhibit promising performance at this task. However, there is significant room for improvement. We expect that future approaches that eschew photorealism and associated losses during training will perform more strongly at this task than existing methods.

2 Related Work

Object Detection. Object detection focuses on identifying and localizing objects within images, with recent deep learning models such as Faster R-CNN [41], YOLO [40] and transformer-based approaches significantly enhancing both accuracy and efficiency [69]. However, occlusion in real-world scenarios like autonomous driving and robotics remains a critical challenge for traditional models. Amodal object detection and segmentation [68, 28] extend traditional approaches by predicting the full projected geometry of partially-occluded objects. In [25], the authors introduced amodal bounding box regression to estimate complete object boundaries, including unseen parts. In [6], the authors used a multi-camera setup and deep networks to jointly learn visible and occluded object segmentations, leveraging contextual cues. More recent approaches improve upon these techniques through cumulative occlusion learning [3]. Unlike amodal object detection and segmentation, which can only reason about partially-occluded objects, we aim to reason about fully-occluded or out-of-frame objects. This requires scene-level priors, not just the object-level priors of amodal methods.

Image Diffusion Models. Diffusion models [51, 18] generate high-quality, plausible images via an iterative denoising process. In conditional generation tasks, like ours, they can be guided from auxiliary inputs such as text or images during the denoising process, known as conditioning [21, 44]. One approach to learning a conditional and unconditional model simultaneously is classifier-free guidance [19], which facilitates applications in scene completion and conditional synthesis [12, 45]. Of relevance to this work is the application of image outpainting, where image boundaries are extended beyond the original content. One highly-successful diffusion model, regularly used for such purposes, is Stable Diffusion [43], which efficiently generates high-resolution images conditioned on text. In this work, we explore what spatio-semantic relationships this model has learned from large-scale image data.

Novel View Synthesis (NVS). NVS is the task of generating new views of a scene from a set of posed input images. Traditional methods like multi-view stereo and structure-from-motion can reconstruct the 3D geometry but may struggle with photorealistic rendering in complex environments [50, 16]. Neural Radiance Fields (NeRF) [31] transformed NVS by using neural networks to parameterize scenes as continuous volumetric radiance fields, enabling high-fidelity rendering. However, NeRF typically requires many input images and known camera poses, limiting its practicality with scarce data. To address this, methods like PixelNeRF [63], PixelSynth [42], and SinNeRF [59] leverage pre-trained scene priors for effective representation from minimal input. While these methods improve generalization to unseen scenes, they still face challenges due to limited viewpoints and lack of geometric constraints, leading to less accurate depth estimation. Recent approaches integrate diffusion models into the NVS pipeline to overcome these issues. Diffusion

with Forward Models (DFM) [55] combines a transformer encoder with PixelNeRF [63, 37] and uses Denoising Diffusion Implicit Models (DDIM) [52] to generate diverse 3D representations conditioned on a single RGB image. GeNVS [10] follows a similar approach, sampling novel views instead of full 3D scenes. Despite its computational demands and challenges with out-of-distribution data, DFM remains a strong benchmark for generating photorealistic, 3D-consistent views from a single image. Although newer models like MultiDiff [32], using depth-warped priors, show improvements both in quality and speed, their implementations were unavailable at the time of this study. In this paper, we investigate the extent to which DFM learns plausible spatio-semantic relationships in 3D.

Vision–Language Models (VLMs). VLMs are effective for spatio-semantic reasoning, excelling in one-shot and zero-shot tasks [11], but struggle with context-based reasoning [65]. Models like CLIP align visual and textual data for object recognition and segmentation [17], yet face challenges with complex spatial relationships, especially in incomplete or sparsely annotated environments [8]. These limitations are evident in tasks requiring spatial reasoning, such as Visual Language Action models [66], and benchmarks like Winoground [11, 62], which highlight difficulties in ambiguous scenes. Visual Question Answering (VQA) systems like ChatGPT and LLaVA [36, 29, 30] have improved multi-modal reasoning but remain limited in understanding 3D spatial relationships [9]. We benchmark several such VLMs, including ChatGPT-4 [36], LLaVA-v1.6-34B [24], Gemini-Pro-Ultra [14], Claude Sonnet 3.5 [2], and QwenVL-Chat [4], in occlusion-heavy and spatially complex environments, to ascertain their ability to understand implicit spatio-semantic relationships in 2D.

3 Unobserved Object Detection

In this section, we define the tasks of 2D and 3D unobserved object detection and outline how existing generative models can be adapted to address this problem. We consider representative 2D and 3D diffusion models, as well as vision–language models, ascertaining how each may be extended to one or both tasks.

3.1 Task Description

The task of unobserved object detection, as shown in Figure 1, is to detect objects that are in the vicinity of, but not observed by, a camera. The approaches considered in this paper address this task by predicting a conditional distribution $\mathcal{D}_{\mathcal{I}}$ over a bounded space and set of semantic labels given a single RGB image \mathcal{I} , referred to as a spatio-semantic distribution (SSD). This facilitates the inference of the probable locations of unobserved objects outside the visible region captured by the image and its associated camera frustum, using contextual cues from the image. The spatial domain \mathcal{X} defines the support of this distribution. The SSD is an estimate of the ground-truth conditional distribution $\Gamma_{\mathcal{I}}$. While this distribution is not observable, we have access to additional posed images from a realization of this conditional distribution for the purposes of evaluation.

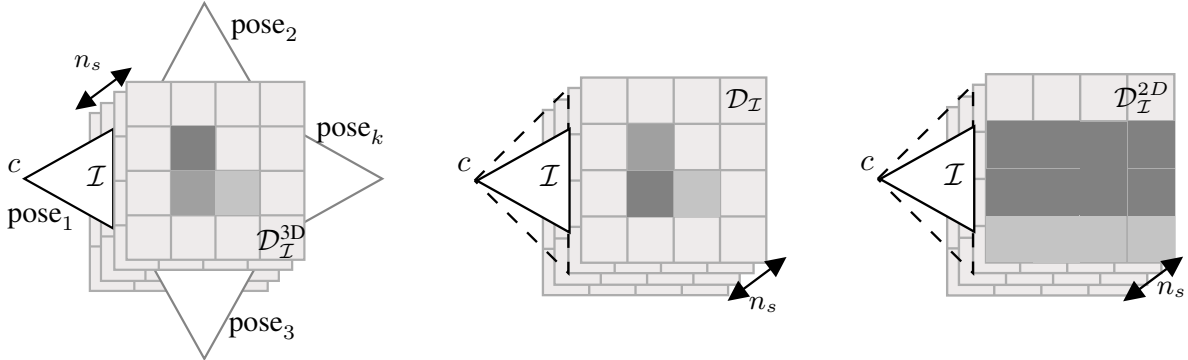
For each object label o , we denote the associated spatial distribution as $\mathcal{D}_{\mathcal{I}o}$. This maps each $x \in \mathcal{X}$ to a likelihood in $[0, 1]$. That is, the likelihood of detecting object o at location x . For example, it assigns a likelihood to the presence of a chair one meter in front of and two meters to the right of the camera, which may not be visible in the input image. Note that we consider all distributions to be normalized.

We consider distributions over two discretized spatial domains \mathcal{X} : (1) a 2D domain \mathbb{I} , discretized as a pixel grid, corresponding to an expansion of the input image; and (2) a 3D domain \mathbb{V} , discretized as a voxel grid, extending beyond the input camera’s frustum. The 2D domain \mathbb{I} symmetrically extends the $H \times W$ pixel grid of the input image to $H \times W'$, where $W' > W$. The 3D domain \mathbb{V} expands the camera frustum to an expanded voxel grid aligned with the camera coordinate system.

3.2 Generative Models for Unobserved Object Detection

This section details how three types of generative model can be extended to estimate the conditional spatio-semantic distribution $\mathcal{D}_{\mathcal{I}o}$ in 2D, 3D or both. The models employed include (1) 3D diffusion models, (2) 2D diffusion models, and (3) vision–language models (VLMs). Detection pipelines derived from these models are deployed in indoor scenes from the RealEstate10k dataset [67] using the MS-COCO dataset [27] object categories.

3D Diffusion. We extend the Diffusion with Forward Models (DFM) [55] model to estimate the conditional distribution. This approach generates a 3D representation conditioned on a single RGB image, from which an RGBD image can be rendered from any camera pose. We select a set of $k = 4$ target poses, including the input image’s pose, as visualized in Figure 2(a), render the corresponding RGBD images, and combine the results into a single point cloud along with the input pose. An off-the-shelf object detector, YOLOv8x [40, 20], is run on the target frames. The 2D bounding boxes for each object o are back-projected onto the point cloud alongside detection confidences. The resulting 3D confidence map is voxelized into grid cells \mathbb{V} , taking the average confidence within each voxel, and is normalized to obtain $\mathcal{D}_{\mathcal{I}}^{3D}$. Since DFM is a generative model, we can take additional samples from the conditional distribution. The above procedure is run for n_s samples, all conditioned on the same input image \mathcal{I} , and the results are aggregated into the estimated distribution by averaging across the samples. As shown visually in Figure 2(a), the DFM detection



(a) The 3D Diffusion pipeline uses novel camera views to generate n_s samples, which are combined to produce $\mathcal{D}_{\mathcal{I}}^{3D}$.

(b) The 2D Diffusion pipeline uses outpainting to generate n_s expanded images used to produce $\mathcal{D}_{\mathcal{I}}^{2D}$ or $\mathcal{D}_{\mathcal{I}}^{3D}$.

(c) A VLM pipeline answers n_s expanded region-wise queries to get $\mathcal{D}_{\mathcal{I}}^{2D}$.

Figure 2: The sampling processes in our proposed detection pipelines based on 2D and 3D diffusion models and VLMs.

pipeline can both expand the detection volume beyond the initial visible frame, as well as recover occlusions using the novel camera views. More details on sampling and rejection processes can be found in Appendix B.

2D Diffusion. To evaluate the capacity of a 2D diffusion model at estimating the conditional distribution, we utilize the SDXL [39] Infinity Runway model to symmetrically extend the 360×360 input image to a 640×360 output. This is achieved by expanding the image canvas to the desired dimensions and performing conditional generation to fill the newly introduced regions through outpainting. We then run an object detector, YOLOv8x [40, 20], for each object o to assign normalized object confidence scores to each pixel, resulting in a 2D spatio-semantic distribution $\mathcal{D}_{\mathcal{I}}^{2D}$ using n_s generated samples (shown in Figure 2(b)). To obtain the estimated 3D distribution $\mathcal{D}_{\mathcal{I}}^{3D}$, the 2D bounding boxes were back-projected into 3D using metric depth values estimated by DepthAnythingv2 [61, 60] and the camera parameters from the dataset, and the result was rescaled to match the ground-truth scale, voxelized and normalized as before. We leveraged DepthAnythingv2 for its superior cross-domain generalizability, given our known camera model.

Vision-Language Models (VLMs). We adapt several VLMs to the task of predicting the (coarsely-discretized) 2D conditional distribution: ChatGPT-4 [36], Claude-3.5 Sonnet [2], Gemini 1.5 Ultra [14], QwenVL-Chat [4], and LLaVa-34B-v1.6 [29]. To do so, each model was provided with the 360×360 input image, padded with 140 black pixels to the left and right, forming a 640×360 image. For each object o , the model was asked whether the object was within the original frame or the extended region to the left or to the right. Model APIs were used for automation, with question order shuffling to avoid bias [15]. To mitigate limitations in large language models, such as uncontrolled token generation [5], responses were constrained to binary response “Yes”/“No”. A consistency score was computed based on 10 repeated queries per region, and the fraction of “Yes” responses was normalized to generate the 2D conditional distribution $\mathcal{D}_{\mathcal{I}}^{2D}$ (Figure 2(c)). Note that the predicted distribution is uniform in each left/center/right region, since the VLM questions only elicit a coarse, region-wise response. Details on the prompts and experiment design are provided in Appendix C.

4 Experiments

In this study, we evaluate model performance on three distinct tasks across 10 different indoor scenes from the RealEstate10k dataset [67]. The benchmarks assess the models’ reasoning abilities in both 2D and 3D contexts, focusing on different aspects of spatial understanding, both within localized regions (the frustum) and for entire scene reconstructions. Metrics have been proposed to evaluate the performance of the detection pipelines against baselines alongside both quantitative and qualitative empirical results.

4.1 Experimental Setup

Dataset. All models are evaluated on 10 scenes from the RealEstate10k test set [67], which were automatically selected based on object detection frequency and an indoor filter. Each of the 10 selected scenes has an average of 134 images with camera pose annotations, after filtering. One frame per scene is used as the input image \mathcal{I} for evaluation. See Appendix A for details on selection criteria, filtering and the input frame timestamps. To generate the ground-truth object distributions, the following procedure was undertaken. Object annotations were generated for every image in the dataset by YOLOv8x [40, 20], pre-trained on MS-COCO [27], chosen for its robustness

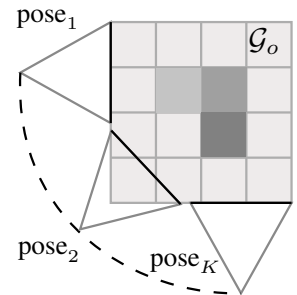


Figure 3: K posed images from an indoor scene of the RealEstate10k dataset are used to produce \mathcal{G}_o^{2D} and \mathcal{G}_o^{3D} .

and generalizability. The normalized object confidences form the 2D ground-truth spatial distributions \mathcal{G}_o^{2D} . Then the 3D structure was estimated using COLMAP [47] triangulation and dense stereo matched reconstruction from the images with their annotated camera poses, followed by outlier filtering (outlined in Figure 3). The 2D bounding boxes were backprojected using the 3D reconstruction, voxelized (averaging confidence values per voxel) and normalized to get the 3D ground-truth spatial distributions, denoted as \mathcal{G}_o^{3D} .

Tasks. This study considers three tasks, denoted as 2D, 2.5D and 3D. The 2D task is to estimate the 2D spatio-semantic distribution $\mathcal{D}_{\mathcal{I}}^{2D}$ within the expanded image domain \mathbb{I} of the input camera view. The 2.5D task is to estimate the part of the spatio-semantic distribution $\mathcal{D}_{\mathcal{I}}^{3D}$ that is visible in the expanded image \mathbb{I} at the input camera location. That is, the distribution of non-occluded surfaces visible at the input, if its field-of-view was wider. Finally, the 3D task is to estimate the spatio-semantic distribution $\mathcal{D}_{\mathcal{I}}^{3D}$, including the occluded regions.

Baselines. We consider two baselines for these tasks: uniform and oracle. For the *uniform* baseline, we assign equal probabilities across the grid. The rationale for this approach is based on the expectation that the distribution is sharper (i.e., lower randomness) near the input and becomes more diffuse further away. For the deterministic *oracle* baseline, we use part of the ground truth that is not available to the other methods. For the 2D task, the oracle receives the true expanded image \mathbb{I} , making its task deterministic object detection. For the 2.5D task, the oracle receives the in-frustum ground-truth distribution that is visible in the expanded input view \mathbb{I} . For the 3D task, the oracle receives the full in-frustum ground-truth distribution. Therefore it knows exactly where the objects are, within the camera’s frustum.

Implementation details. The images in the RealEstate10k dataset [67] have dimension 360×640 from which the input images \mathcal{I} are center-cropped to 360×360 . One input image is selected per scene, forming a set of 10 scenes \mathcal{S} . A set of 10 COCO objects \mathcal{O} was selected based on their frequency in the RealEstate10k dataset (see Appendix A). DFM [55] inference was modified to reduce the number of intermediate steps for faster autoregressive sampling, with a temperature of 0.85 and a guidance scale of 2.0. For SDXL, we padded the input image by 140 pixels to the left and right for masked inpainting, used a temperature of 0.25 and prompt guidance scales of 0.25, 0.5, 0.75, and 1.0, generating 50 samples per scale. YOLOv8x detections were filtered with a minimum confidence threshold of 0.1 and an NMS threshold of 0.85. For VLM models, the temperature was set to 0.25, the top-p parameter was set to 1.0 and a fixed seed of 42 was used for reproducibility. Due to time constraints and access limitations, all VLM APIs were sampled in parallel, taking a total of 18 hours. All experiments were conducted on a single NVIDIA RTX A6000, and all code, data, and evaluation protocols will be publicly released.

4.2 Metrics for unobserved object detection

In order to evaluate the unobserved object detection task, we propose several metrics to quantify how well the predicted conditional distribution $\mathcal{D}_{\mathcal{I}o}$ for object o over a discrete domain \mathcal{X} conforms to the true conditional distribution. However, we only have access to a single realization of this conditional distribution, denoted \mathcal{G}_o , which we assume to be available. The procedure for constructing this ground-truth distribution is detailed in Appendix A. Significantly, the true conditional distribution $\Gamma_{\mathcal{I}o}$ is likely to have more modes than the realization \mathcal{G}_o . For example, given an image \mathcal{I} of a dining table, the ground-truth scene (the realization) happened to have several chairs clustered to the right of the camera. However, the exact same image could equally well have corresponded to a scene with a chair to the left of the camera (another, unrealized, scene conditioned on the same image). We expect the models to predict all plausible modes, and this asymmetry between the ground-truth and the prediction informs our choice of metrics.

Normalized Entropy \mathcal{H} and Normalized Cross-Entropy \mathcal{H}^\times . To quantify how close the predicted distribution is to a uniform distribution, a maximally uncertain prediction, we report the Shannon entropy [49] \mathcal{H} , normalized such that $\mathcal{H} \in [0, 1]$ and a uniform distribution evaluates to $\mathcal{H} = 1$. We also report the normalized cross-entropy \mathcal{H}^\times between the ground-truth distribution \mathcal{G}_o and the predicted distribution $\mathcal{D}_{\mathcal{I}o}$. This asymmetric measure penalizes the prediction of low object likelihood where the ground-truth indicates the presence of an object. However, as required, it does not penalize the prediction of high object likelihoods where the ground-truth has not seen an object. These metrics are given by

$$\mathcal{H} = -\frac{1}{|\mathcal{S}||\mathcal{O}|\log|\mathcal{X}|} \sum_{\mathcal{I} \in \mathcal{S}} \sum_{o \in \mathcal{O}} \sum_{x \in \mathcal{X}} \mathcal{D}_{\mathcal{I}o}(x) \log \mathcal{D}_{\mathcal{I}o}(x) \quad (1)$$

$$\mathcal{H}^\times = -\frac{1}{|\mathcal{S}||\mathcal{O}|\log|\mathcal{X}|} \sum_{\mathcal{I} \in \mathcal{S}} \sum_{o \in \mathcal{O}} \sum_{x \in \mathcal{X}} \mathcal{G}_o(x) \log \mathcal{D}_{\mathcal{I}o}(x), \quad (2)$$

where \mathcal{O} is the set of objects and \mathcal{S} is the set of input images (equal to the set of scenes).

Normalized Nearest Neighbor Distance \mathcal{D}^{NN} . We define a metric to quantify the spatial distance between ground-truth object locations and the nearest high-likelihood prediction. To this end, the distances between peaks in \mathcal{G}_o (i.e., locations containing object o) and the nearest high-likelihood location in $\mathcal{D}_{\mathcal{I}o}$ are computed. Large distances on average

Table 1: Performance of all models on the 2D unobserved object detection task. We report the normalized cross-entropy \mathcal{H}^\times , the normalized nearest neighbor distance \mathcal{D}^{NN} , the percentage of false negatives (FN), the prediction entropy \mathcal{H} and the region-wise classification accuracy \mathcal{A} . For DFM, the number of conditionally-independent samples n_s per input image is reported, as is the number of rendered camera poses k ; the total number of samples per input image is therefore kn_s . The best non-baseline result is indicated in bold.

| Methods | $\mathcal{H}^\times \downarrow$ | $\mathcal{D}^{\text{NN}}\% \downarrow$ | 2D Task | | $\mathcal{A} \uparrow$ |
|---------------------------|---------------------------------|--|------------------|--------------------------|------------------------|
| | | | FN% \downarrow | $\mathcal{H} \downarrow$ | |
| Baseline-uniform | 0.25 | 0.00 | 0.00 | 1.00 | 0.08 |
| Baseline-oracle | 0.00 | 0.00 | 0.00 | 0.14 | 1.00 |
| DFM ($n_s = 25, k = 4$) | 1.96 | 0.00 | 0.00 | 0.72 | 0.38 |
| DFM ($n_s = 25, k = 3$) | 2.01 | 2.08 | 0.21 | 0.83 | 0.34 |
| DFM ($n_s = 25, k = 2$) | 2.18 | 3.72 | 0.28 | 0.87 | 0.35 |
| DFM ($n_s = 15, k = 4$) | 2.91 | 6.51 | 2.27 | 0.84 | 0.19 |
| DFM ($n_s = 10, k = 4$) | 3.72 | 9.16 | 8.12 | 0.92 | 0.11 |
| SDXL (w/ obj prompts) | 1.43 | 11.55 | 2.63 | 0.84 | 0.47 |
| SDXL (w/o obj prompts) | 3.61 | 17.11 | 31.58 | 0.92 | 0.28 |
| SDXL (w/o prompts) | 6.54 | 31.58 | 86.32 | 0.97 | 0.12 |
| ChatGPT-4 | 1.22 | 0.00 | 2.63 | 0.99 | 0.62 |
| Claude-Sonnet-3.5 | 1.31 | 0.00 | 0.00 | 0.99 | 0.65 |
| Gemini 1.5 Ultra | 2.21 | 0.12 | 2.63 | 0.98 | 0.57 |
| QwenVL-Chat | 2.58 | 0.51 | 10.53 | 0.98 | 0.54 |
| LLaVa-v1.6-34b | 1.56 | 0.08 | 7.89 | 0.98 | 0.57 |

are indicative of a predictor that is failing to assign high likelihoods to locations where the object was observed in the ground truth. This metric is given by

$$\mathcal{D}^{\text{NN}} = \frac{1}{|\mathcal{S}||\mathcal{O}||P_{\mathcal{G}_o}|} \sum_{\mathcal{I} \in \mathcal{S}} \sum_{o \in \mathcal{O}} \sum_{x \in P_{\mathcal{G}_o}} \min_{y \in P_{\mathcal{D}_{\mathcal{I}o}}} \frac{\|x - y\|}{\text{diam}(\mathcal{X})}, \quad (3)$$

where $P_{\mathcal{G}_o}$ is the set of peaks or modes in \mathcal{G}_o , $P_{\mathcal{D}_{\mathcal{I}o}} = \{x \in \mathcal{X} \mid \mathcal{D}_{\mathcal{I}o}(x) \geq 1/|\mathcal{X}|\}$ is the set of high-likelihood locations in $\mathcal{D}_{\mathcal{I}o}$, and $\text{diam}(\mathcal{X})$ is the maximum distance within \mathcal{X} (e.g., the diagonal or space diagonal for a 2D or 3D grid) that normalizes the measure with respect to the domain size.

Region-wise Classification Accuracy \mathcal{A} . This metric evaluates the coarse-grained accuracy of a predictor by decomposing the domain \mathcal{X} into $\ell = 3$ regions and measuring the classification accuracy. Specifically, we divide the domain into subdomains \mathcal{X}^i , corresponding to the left-of-image, within-image and right-of-image regions. The metric is given by

$$\mathcal{A} = \frac{1}{\ell|\mathcal{S}||\mathcal{O}|} \sum_{\mathcal{I} \in \mathcal{S}} \sum_{o \in \mathcal{O}} \sum_{i=1}^{\ell} y_o^i \hat{y}_o^i + (1 - y_o^i)(1 - \hat{y}_o^i), \quad (4)$$

where y_o^i is the ground-truth label for object o in region i (1 if the object is present and 0 otherwise), and $\hat{y}_o^i = \max_{x \in \mathcal{X}^i} [\mathcal{D}_{\mathcal{I}o}(x) \geq 1/|\mathcal{X}^i|]$ is the predicted label, with $[\cdot]$ denoting Iverson brackets.

4.3 Results

In this section, we report the results of a comprehensive evaluation of the generative models at the 2D, 2.5D and 3D unobserved object detection tasks, as shown in Tables 1 and 2. Alongside the metrics outlined in Section 4.2, we also report the percentage of false negatives (FN), defined as the proportion of instances where the predicted distribution fails to identify the presence of the object, despite its presence in the ground truth. Note that before averaging over the dataset, statistical outliers were filtered, identified as those above $Q_3 + 1.5\text{IQR}$. Methods were only evaluated on tasks for which they are applicable. For example, VLMs could not be evaluated on the 3D tasks, since they only provide 1D information (left, center, right).

For the 2D task (Table 1), we see that the 3D diffusion method (DFM) has the best performance with respect to all metrics other than the classification accuracy and the cross-entropy, for which the VLMs tend to perform better. For the 2.5D task (Table 2, left), we see that the 3D diffusion model consistently outperforms the 2D diffusion model (SDXL) augmented with monocular depth predictions, except on the accuracy metric. Finally, for the 3D task (Table 2, right), we see that the 3D diffusion model has clear superiority over all other applicable methods, including the oracle baseline,

Table 2: Performance of all models on the 2.5D and 3D unobserved object detection tasks. We report the normalized cross-entropy \mathcal{H}^\times , the normalized nearest neighbor distance \mathcal{D}^{NN} , the percentage of false negatives (FN), the prediction entropy \mathcal{H} and the region-wise classification accuracy \mathcal{A} . The best non-baseline result is indicated in bold.

| Methods | 2.5D Task | | | | | 3D Task | | | |
|---------------------------|---------------------------------|--|------------------|--------------------------|------------------------|---------------------------------|--|------------------|--------------------------|
| | $\mathcal{H}^\times \downarrow$ | $\mathcal{D}^{\text{NN}}\% \downarrow$ | FN% \downarrow | $\mathcal{H} \downarrow$ | $\mathcal{A} \uparrow$ | $\mathcal{H}^\times \downarrow$ | $\mathcal{D}^{\text{NN}}\% \downarrow$ | FN% \downarrow | $\mathcal{H} \downarrow$ |
| Baseline-uniform | 1.72 | 0.00 | 0.00 | 1.00 | 0.08 | 2.32 | 0.00 | 0.00 | 1.00 |
| Baseline-oracle | 0.00 | 0.00 | 0.00 | 0.24 | 1.00 | 3.11 | 19.84 | 43.75 | 0.71 |
| DFM ($n_s = 25, k = 4$) | 0.15 | 1.18 | 0.00 | 0.74 | 0.38 | 1.66 | 0.03 | 12.75 | 0.43 |
| DFM ($n_s = 25, k = 3$) | 0.18 | 2.17 | 0.21 | 0.83 | 0.34 | 2.14 | 3.11 | 31.72 | 0.47 |
| DFM ($n_s = 25, k = 2$) | 1.71 | 2.45 | 0.28 | 0.88 | 0.35 | 2.77 | 6.32 | 36.85 | 0.54 |
| DFM ($n_s = 15, k = 4$) | 2.04 | 1.55 | 2.27 | 0.77 | 0.19 | 2.98 | 0.14 | 33.45 | 0.50 |
| DFM ($n_s = 10, k = 4$) | 2.82 | 6.13 | 8.12 | 0.82 | 0.11 | 4.33 | 1.89 | 45.12 | 0.62 |
| SDXL (w/ obj prompts) | 1.48 | 9.04 | 2.63 | 0.82 | 0.47 | – | – | – | – |
| SDXL (w/o obj prompts) | 2.48 | 7.86 | 31.58 | 0.86 | 0.28 | – | – | – | – |
| SDXL (w/o prompts) | 8.25 | 13.23 | 86.32 | 0.94 | 0.12 | – | – | – | – |

which has access to the ground truth within the frustum of the input image’s camera. This highlights the importance for this task of generating plausible predictions beyond what can be seen in the input.

Qualitative results are shown in Figure 4, with the 360×360 center-cropped input image \mathcal{I} shown within the dashed lines in the first column, a top-down view of the DFM-predicted 3D distribution in the second column, the SDXL-predicted 2D distribution in the third column, and the ChatGPT-predicted 2D distribution in the last column. We observe that all methods infer relatively sensible distributions. In particular, the DFM-based model usually predicts high likelihoods near the ground-truth object’s 3D location, including when the object is occluded or out-of-frame, which is a significantly harder task than the 2D prediction task; see, for example, the final row. Failure cases are shown in Figure 5, including hard examples where objects are behind the camera and an object category (door) that elicits many false negatives in the object detector. We also observe that the diffusion-based outpainting approach has its own modes of failure, as shown in Figure 6. In particular, if the outpainting model is not prompted with the label of the object to be detected, the results tend to be uninformative about the scene.

4.4 Analysis & Ablation Study

This section presents an analysis of the 3D diffusion model based on DFM [55] and an ablation study for the 2D diffusion model based on SDXL [39]. First, as reported in Tables 1 and 2, we analyze the effect of reducing the number of camera poses k at which the DFM model is queried, from 4 to 2, which affects the coverage of the scene. To do so, we randomly drop out one or two camera poses and report the average results. We find that the performance decreases considerably as the number of query camera poses decreases, across all tasks. Second, we analyze the effect of reducing the number of conditionally-independent samples n_s per input image from 25 to 10, which reduces the diversity of the predicted conditional distribution. This also leads to a significant performance decrease, since the predicted distribution is less able to model the modes of the true conditional distribution.

We also ablate the 2D diffusion-based approach, investigating the effect of text prompts on the results, as reported in Tables 1 and 2. We consider three alternatives: (a) without text prompts; (b) without object prompts, where the model is provided with text guidance but without reference to any objects (e.g., “extend this indoor scene naturally to the left and right of the given frame”); and (c) with object prompts, where the model is provided with object-specific prompts (e.g., “extend this scene naturally on both sides, with objects like [OBJECT]”). The results indicate that object prompts are critical to the performance of the outpainting-based method, which suggests that the model is not making good use of the visual information in the input image.

5 Discussion and Conclusion

Limitations. This work has several significant limitations. In particular, the inference time of generative models, especially 3D diffusion models, is currently very large. Since our approaches require many samples to approximate the conditional distribution, this is a significant bottleneck and stymies their use in real-time applications like in robotics. Another limitation is the need for object prompts for the outpainting-based methods, since this is likely to bias the obtained empirical conditional distribution. Also, the VLM-based approach evaluations may not be fully reliable, since it is possible these models have seen test set images during training and so could have memorized the uncropped images.

Conclusion. This work has introduced unobserved object detection in 2D and 3D, presented three detection pipelines using state-of-the-art generative models, and evaluated their performance on a proposed set of metrics in a dataset of indoor scenes and common objects. We find that unobserved object detection presents different characteristics in 2D

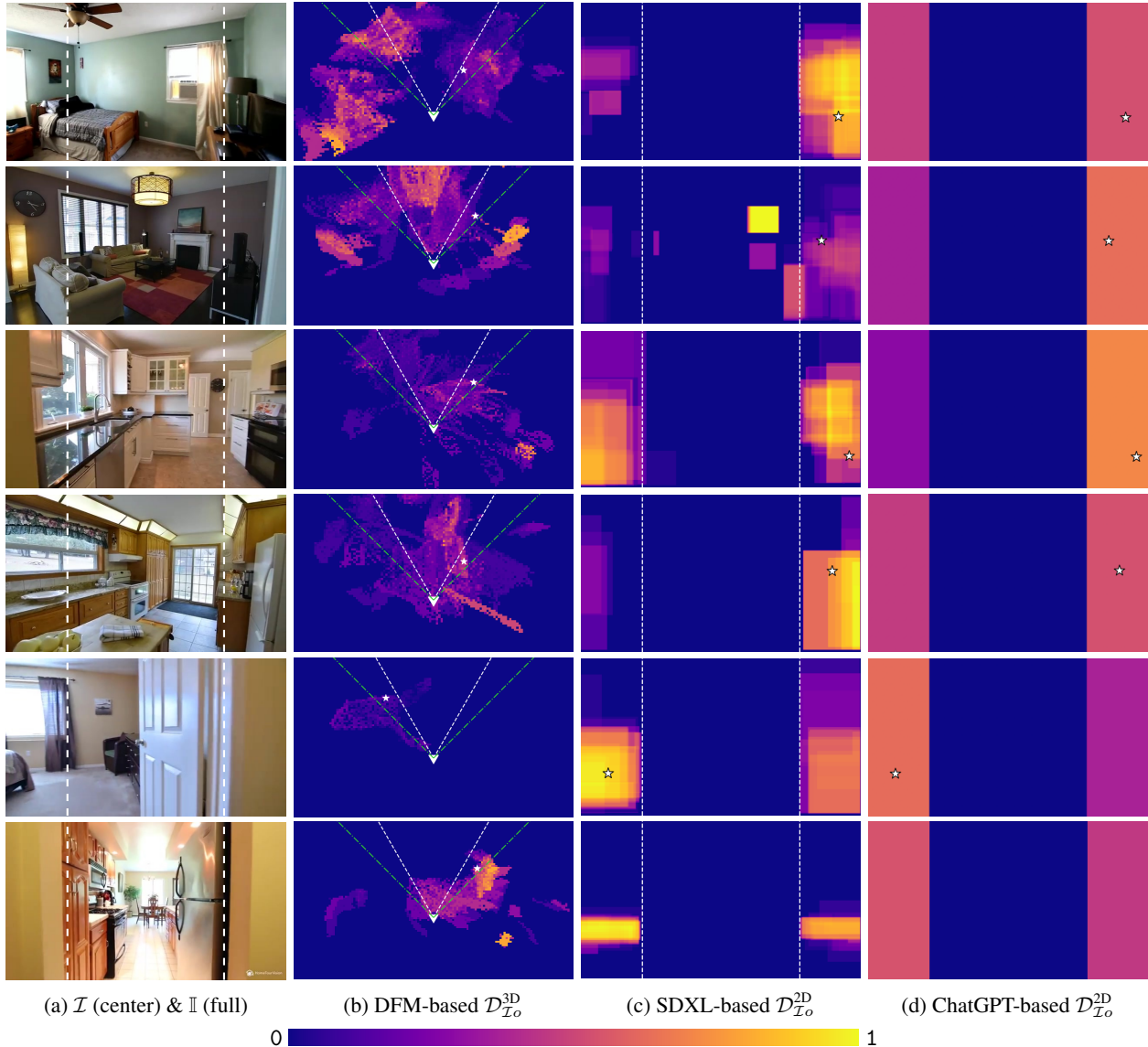
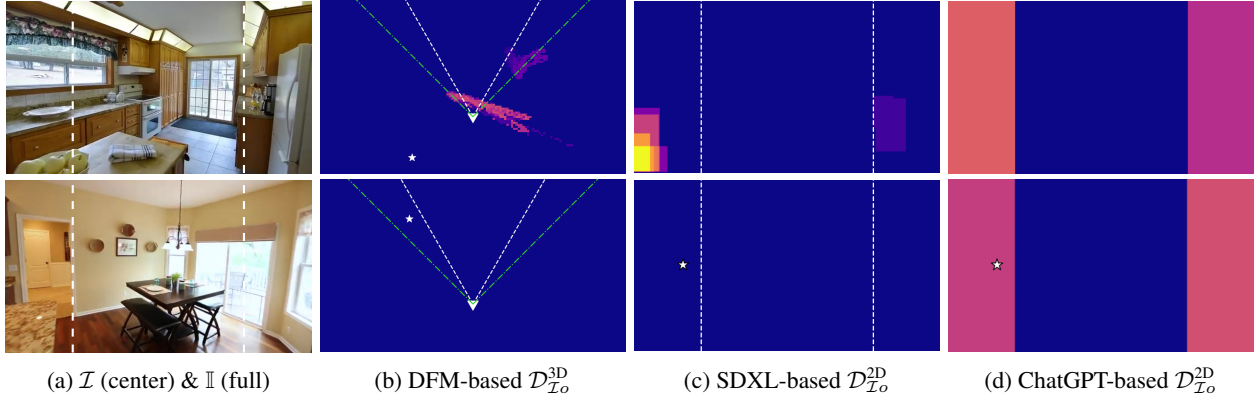


Figure 4: Qualitative results. Each row presents the predicted 2D and 3D spatial distributions (the latter is projected top-down for clarity) generated by each method. The object categories include TV (first and second rows), oven (third row), refrigerator (fourth row), bed (fifth row), and sink (sixth row). The bottom row is of particular interest: the DFM-based model is able to infer the likely presence of a sink behind and to the right of the refrigerator. The heatmap colors represent the object likelihood at that location (warmer is more likely), and the heatmaps in column (c) use a logarithmic scale. The camera position is marked by a white triangle, the camera frustums associated with \mathcal{I} and \mathbb{I} are drawn with dashed and dot-dashed lines respectively, and the object location is marked by a white star, when visible.

and 3D. Expanding the camera frame can be used in both 2D and 3D, with detection pipelines showing the ability to predict objects that may be fully outside the visible frustum. In contrast, predicting objects within 3D regions larger than the camera frustum implies the ability of such 3D pipelines to detect fully-occluded objects. In this work, the 2D pipelines based on outpainting and VLMs are unable to detect occluded objects, while the 3D pipeline based on a 3D diffusion model can do so. Handling occlusions is a particular capability motivated by unobserved object detection.

Future work. While the work presents a promising initial step towards this significant task, it also sets up some open questions. For example, while all of the detection pipelines presented in this work use pre-trained generative models, it is likely that training for this task directly would elicit more accurate predictions. Moreover, the 2D and 3D diffusion models are repurposed from their original task of photorealistic generation, but it is unclear whether high-fidelity generation is desirable for unobserved object detection. One might expect it to be simpler to train a model to directly generate samples from the conditional spatio-semantic distribution at lower resolutions. Finally, future work could explore how unobserved object detection interacts with downstream tasks, such as robot reactive control to choose



(a) \mathcal{I} (center) & \mathbb{I} (full) (b) DFM-based $\mathcal{D}_{\mathcal{I}o}^{3D}$ (c) SDXL-based $\mathcal{D}_{\mathcal{I}o}^{2D}$ (d) ChatGPT-based $\mathcal{D}_{\mathcal{I}o}^{2D}$

Figure 5: Failure cases. In the first row, the DFM-based model incorrectly predicts a chair directly in front of the camera, despite none being present, and fails to detect a chair located behind the camera. In the second row, the presence of the door on the left is not inferred by the DFM- or SDXL-based models, largely due to object detector false negatives.



(a) (b) (c)

Figure 6: Outpainting failure cases. The SDXL outpainting model, under the “without object prompts” setting, often extends images with textures (a) or unrelated imagery (b). When object prompts (here, “refrigerator”) are provided (c), the results may still ignore the prompt and generate unnatural extended images.

between going forward, left, or right, where coarse-grained spatial resolutions are likely to be sufficient, or visual search and long-horizon probabilistic planning, where relatively fine-grained spatial resolutions may be needed.

Ethics Statement. Approaches, like ours, that address the task of unobserved object detection may lead to potential societal benefits, such as through making autonomous systems more capable and better able to reason about their surroundings. However, there are several potential concomitant risks with systems that can infer information that has not been observed. This could include indirect privacy violations and unfair decisions made using predictions from a model that may be biased due to its training data or strategy. To mitigate the effect of this, we make use of publicly-available pre-trained models and datasets, so that potential risks can be investigated and quantified. Additionally, to mitigate the environmental impact of training large generative models, we use pre-trained models and optimize computational resources wherever possible.

Reproducibility Statement. The code for our experiments, including data pre-processing, sampling, detection, and evaluation pipelines, will be made publicly available, along with detailed setup instructions, dependencies, and all hyperparameters. The dataset used is publicly accessible, and all necessary configurations for model and data processing are provided to ensure replication. However, one part of our study depends on third-party closed vision-language models accessed via APIs, which may be updated, leading to potential variations in results. While we document the specific API versions, configurations and access dates, changes in these services or access limitations may impact exact reproducibility.

References

- [1] Michal Adamkiewicz, Timothy Chen, Adam Caccavale, Rachel Gardner, Preston Culbertson, Jeannette Bohg, and Mac Schwager. Vision-Only Robot Navigation in a Neural Radiance World. *IEEE Robotics and Automation Letters*, 7(2):4606–4613, 2022.
- [2] Anthropic. The Claude 3 Model Family: Opus, Sonnet, Haiku. https://www-cdn.anthropic.com/de8ba9b01c9ab7cbabf5c33b80b7bbc618857627/Model_Card_Claude_3.pdf, 2023.
- [3] Jiayang Ao, Qihong Ke, and Krista A. Ehinger. Sequential Amodal Segmentation via Cumulative Occlusion Learning. *arXiv preprint arXiv:2405.05791*, 2024.

- [4] Jinze Bai, Shuai Bai, Shusheng Yang, Shijie Wang, Sinan Tan, Peng Wang, Junyang Lin, Chang Zhou, and Jingren Zhou. Qwen-VL: A Versatile Vision-Language Model for Understanding, Localization, Text Reading, and Beyond. *arXiv preprint arXiv:2308.12966*, 2023.
- [5] Sourav Banerjee, Ayushi Agarwal, and Saloni Singla. LLMs Will Always Hallucinate, and We Need to Live With This. *arXiv preprint arXiv:2409.05746*, 2024.
- [6] Pierre Baqué, François Fleuret, and Pascal Fua. Deep Occlusion Reasoning for Multi-Camera Multi-Target Detection. *arXiv preprint arXiv:1704.05775*, 2017.
- [7] Miguel Ángel Bautista, Pengsheng Guo, Samira Abnar, Walter Talbott, Alexander T Toshev, Zhuoyuan Chen, Laurent Dinh, Shuangfei Zhai, Hanlin Goh, Daniel Ulbricht, Afshin Dehghan, and Joshua M. Susskind. GAUDI: A Neural Architect for Immersive 3D Scene Generation. In *Proceedings of the Neural Information Processing Conference*, 2022.
- [8] Florian Bordes, Richard Yuanzhe Pang, Anurag Ajay, Alexander C Li, Adrien Bardes, Suzanne Petryk, Oscar Ma textasciitilde nas, Zhiqiu Lin, Anas Mahmoud, Bargav Jayaraman, et al. An Introduction to Vision-Language Modeling. *arXiv preprint arXiv:2405.17247*, 2024.
- [9] Florian Bordes, Shashank Shekhar, Mark Ibrahim, Diane Bouchacourt, Pascal Vincent, and Ari Morcos. PUG: Photorealistic and Semantically Controllable Synthetic Data for Representation Learning. In A. Oh, T. Naumann, A. Globerson, K. Saenko, M. Hardt, and S. Levine, editors, *Advances in Neural Information Processing Systems (NeurIPS)*, volume 36, pages 45020–45054. Curran Associates, Inc., 2023.
- [10] Eric R. Chan, Koki Nagano, Matthew A. Chan, Alexander W. Bergman, Jeong Joon Park, Axel Levy, Miika Aittala, Shalini De Mello, Tero Karras, and Gordon Wetzstein. Generative Novel View Synthesis with 3D-Aware Diffusion Models. In *Proceedings of the IEEE/CVF International Conference on Computer Vision*, pages 4217–4229, October 2023.
- [11] Boyuan Chen, Zhuo Xu, Sean Kirmani, Brian Ichter, Danny Driess, Pete Florence, Dorsa Sadigh, Leonidas Guibas, and Fei Xia. SpatialVLM: Endowing Vision-Language Models with Spatial Reasoning Capabilities. In *Proceedings of the IEEE/CVF Conference on Computer Vision and Pattern Recognition*, June 2024.
- [12] Hyungjin Chung, Jeongsol Kim, Michael Thompson Mccann, Marc Louis Klasky, and Jong Chul Ye. Diffusion posterior sampling for general noisy inverse problems. In *International Conference on Learning Representations*, 2023.
- [13] Yasutaka Furukawa and Jean Ponce. Accurate, dense, and robust multiview stereopsis. *Transactions on Pattern Analysis and Machine Intelligence*, 2010.
- [14] Gemini Team Google Research. Gemini: A Family of Highly Capable Multimodal Models. *arXiv preprint arXiv:2312.11805*, 2024.
- [15] Vipul Gupta, David Pantoja, Candace Ross, Adina Williams, and Megan Ung. Changing Answer Order Can Decrease MMLU Accuracy. *arXiv preprint arXiv:2406.19470*, 2024.
- [16] Richard Hartley and Andrew Zisserman. *Multiple View Geometry in Computer Vision*. Cambridge University Press, 2003.
- [17] Jack Hessel, Ari Holtzman, Maxwell Forbes, Ronan Le Bras, and Yejin Choi. CLIPScore: A Reference-free Evaluation Metric for Image Captioning. In *EMNLP*, 2021.
- [18] Jonathan Ho, Ajay Jain, and Pieter Abbeel. Denoising Diffusion Probabilistic Models. In *Advances in Neural Information Processing Systems (NeurIPS)*, volume 33, pages 6840–6851, 2020.
- [19] Jonathan Ho and Tim Salimans. Classifier-Free Diffusion Guidance. *arXiv preprint*, 2022.
- [20] Glenn Jocher, Ayush Chaurasia, and Jing Qiu. Ultralytics YOLOv8, 2023.
- [21] Gwanghyun Kim, Taesung Kwon, and Jong Chul Ye. DiffusionCLIP: Text-Guided Diffusion Models for Robust Image Manipulation. In *Proceedings of the IEEE/CVF Conference on Computer Vision and Pattern Recognition*, pages 2426–2435, 2022.
- [22] Diederik P. Kingma, Tim Salimans, Ben Poole, and Jonathan Ho. Variational Diffusion Models. In *Advances in Neural Information Processing Systems*, pages 21696–21707, 2021.
- [23] Hanna Kurniawati. Partially observable markov decision processes and robotics. *Annual Review of Control, Robotics, and Autonomous Systems*, 5(1):253–277, 2022.
- [24] Bo Li, Kaichen Zhang, Hao Zhang, Dong Guo, Renrui Zhang, Feng Li, Yuanhan Zhang, Ziwei Liu, and Chunyuan Li. LLaVA-NeXT: Stronger LLMs Supercharge Multimodal Capabilities in the Wild, May 2024.
- [25] Y. Li and J. Malik. Amodal Instance Segmentation. In *European Conference on Computer Vision (ECCV)*, 2016.

- [26] Yikang Li, Wanli Ouyang, Bolei Zhou, Kun Wang, and Xiaogang Wang. Scene graph generation from objects, phrases and region captions. In *Proceedings of the IEEE international Conference on Computer Vision*, pages 1261–1270, 2017.
- [27] Tsung-Yi Lin, Michael Maire, Serge Belongie, James Hays, Pietro Perona, Deva Ramanan, Piotr Dollár, and C Lawrence Zitnick. Microsoft COCO: Common objects in context. In *Computer Vision—ECCV 2014: 13th European Conference, Zurich, Switzerland, September 6–12, 2014, Proceedings, Part V 13*, pages 740–755. Springer, 2014.
- [28] Huan Ling, David Acuna, Karsten Kreis, Seung Wook Kim, and Sanja Fidler. Variational amodal object completion. *Advances in Neural Information Processing Systems (NeurIPS)*, 33:16246–16257, 2020.
- [29] Haotian Liu, Chunyuan Li, Yuheng Li, and Yong Jae Lee. Improved Baselines with Visual Instruction Tuning. *arXiv preprint arXiv:2310.03744*, 2023.
- [30] Haotian Liu, Chunyuan Li, Yuheng Li, Bo Li, Yuanhan Zhang, Sheng Shen, and Yong Jae Lee. LLaVA-NeXT: Improved reasoning, OCR, and world knowledge, January 2024.
- [31] Ben Mildenhall, Pratul P. Srinivasan, Matthew Tancik, Jonathan T. Barron, Ravi Ramamoorthi, and Ren Ng. NeRF: Representing Scenes as Neural Radiance Fields for View Synthesis. In *Proceedings of the European Conference on Computer Vision*, 2020.
- [32] Norman Müller, Katja Schwarz, Barbara Rössle, Lorenzo Porzi, Samuel Rota Bulò, Matthias Nießner, and Peter Kotschieder. MultiDiff: Consistent Novel View Synthesis from a Single Image. In *Proceedings of the IEEE/CVF Conference on Computer Vision and Pattern Recognition*, pages 10258–10268, June 2024.
- [33] Raul Mur-Artal, Jose Maria Martinez Montiel, and Juan D Tardos. ORB-SLAM: A Versatile and Accurate Monocular SLAM System. *IEEE Transactions on Robotics*, 31(5):1147–1163, 2015.
- [34] Raúl Mur-Artal and Juan D Tardós. ORB-SLAM2: An Open-Source SLAM System for Monocular, Stereo, and RGB-D Cameras. In *IEEE Transactions on Robotics*, volume 33, pages 1255–1262. IEEE, 2017.
- [35] Keiko Nagami and Mac Schwager. State Estimation and Belief Space Planning Under Epistemic Uncertainty for Learning-Based Perception Systems. *IEEE Robotics and Automation Letters*, 9(6):5118–5125, 2024.
- [36] OpenAI. GPT-4 Technical Report. *arXiv preprint arXiv:2303.08774*, 2023.
- [37] William Peebles and Saining Xie. Scalable Diffusion Models with Transformers. *arXiv preprint arXiv:2212.09748*, 2023.
- [38] Sergio Pertuz, Daniel Puig, and Miguel A. Garcia. Analysis of Focus Measure Operators for Shape-from-Focus. *Pattern Recognition (PR)*, 46(5):1415–1432, 2013.
- [39] Dustin Podell, Zion English, Kyle Lacey, Andreas Blattmann, Tim Dockhorn, Jonas Müller, Joe Penna, and Robin Rombach. SDXL: Improving Latent Diffusion Models for High-Resolution Image Synthesis. In *The Twelfth International Conference on Learning Representations*, 2024.
- [40] Joseph Redmon, Santosh Divvala, Ross Girshick, and Ali Farhadi. You Only Look Once: Unified, Real-Time Object Detection. In *Proceedings of the IEEE Conference on Computer Vision and Pattern Recognition*, pages 779–788, 2016.
- [41] Shaoqing Ren, Kaiming He, Ross Girshick, and Jian Sun. Faster R-CNN: Towards real-time object detection with region proposal networks. *IEEE Transactions on Pattern Analysis and Machine Intelligence (TPAMI)*, 39(6):1137–1149, 2016.
- [42] Chris Rockwell, David F Fouhey, and Justin Johnson. Pixelsynth: Generating a 3D-consistent Experience From a Single Image. In *Proceedings of the International Conference on Computer Vision*, 2021.
- [43] Robin Rombach, Andreas Blattmann, Dominik Lorenz, Patrick Esser, and Björn Ommer. High-resolution image synthesis with latent diffusion models. In *Proceedings of the IEEE/CVF Conference on Computer Vision and Pattern Recognition*, pages 10684–10695, 2022.
- [44] Chitwan Saharia, William Chan, Huiwen Chang, Chris Lee, Jonathan Ho, Tim Salimans, David Fleet, and Mohammad Norouzi. Palette: Image-to-image diffusion models. *ACM Transactions on Graphics*, pages 1–10, 2022.
- [45] Chitwan Saharia, William Chan, Saurabh Saxena, Lala Li, Jay Whang, Emily Denton, Seyed Kamyar Seyed Ghasemipour, Raphael Gontijo-Lopes, Burcu Karagol Ayan, Tim Salimans, Jonathan Ho, David J. Fleet, and Mohammad Norouzi. Photorealistic Text-to-Image Diffusion Models with Deep Language Understanding. In *Proceedings of the Neural Information Processing Conference*, 2022.

- [46] Kyle Sargent, Zizhang Li, Tanmay Shah, Charles Herrmann, Hong-Xing Yu, Yunzhi Zhang, Eric Ryan Chan, Dmitry Lagun, Li Fei-Fei, Deqing Sun, and Jiajun Wu. ZeroNVS: Zero-Shot 360-Degree View Synthesis from a Single Image. In *Proceedings of the IEEE/CVF Conference on Computer Vision and Pattern Recognition*, pages 9420–9429, June 2024.
- [47] Johannes Lutz Schönberger and Jan-Michael Frahm. Structure-from-motion revisited. In *Proceedings of the IEEE/CVF Conference on Computer Vision and Pattern Recognition*, pages 4104–4113, 2016.
- [48] Dhruv Shah, Ajay Sridhar, Nitish Dashora, Kyle Stachowicz, Kevin Black, Noriaki Hirose, and Sergey Levine. ViNT: A Foundation Model for Visual Navigation. In *7th Annual Conference on Robot Learning*, 2023.
- [49] Claude E. Shannon. A Mathematical Theory of Communication. *Bell System Technical Journal*, 27(3):379–423, 1948.
- [50] Noah Snavely, Steven M Seitz, and Richard Szeliski. Photo tourism: exploring photo collections in 3D. In *ACM Transactions on Graphics*, pages 835–846, 2006.
- [51] Jascha Sohl-Dickstein, Eric Weiss, Niru Maheswaranathan, and Surya Ganguli. Deep unsupervised learning using nonequilibrium thermodynamics. In *International Conference on Machine Learning*, pages 2256–2265. PMLR, 2015.
- [52] Jiaming Song, Chenlin Meng, and Stefano Ermon. Denoising Diffusion Implicit Models. *International Conference on Learning Representations*, 2021.
- [53] Shuran Song, Fisher Yu, Andy Zeng, Angel X Chang, Manolis Savva, and Thomas Funkhouser. Semantic scene completion from a single depth image. In *Proceedings of the IEEE Conference on Computer Vision and pattern recognition*, pages 1746–1754, 2017.
- [54] Y. Song and S. Ermon. Score-based generative modeling through stochastic differential equations. In *International Conference on Learning Representations*, 2021.
- [55] Ayush Tewari, Tianwei Yin, George Cazenavette, Semon Rezhikov, Joshua B. Tenenbaum, Fredo Durand, William T. Freeman, and Vincent Sitzmann. Diffusion with Forward Models: Solving Stochastic Inverse Problems Without Direct Supervision. In *Thirty-seventh Conference on Neural Information Processing Systems*, 2023.
- [56] Z. Wang, A. C. Bovik, H. R. Sheikh, and E. P. Simoncelli. Image quality assessment: From error visibility to structural similarity. *IEEE Transactions on Image Processing*, 13(4):600–612, 2004.
- [57] Daniel Watson, William Chan, Ricardo Martin-Brualla, Jonathan Ho, Andrea Tagliasacchi, and Mohammad Norouzi. Novel View Synthesis With Diffusion Models. *International Conference on Learning Representations*, 2023.
- [58] Chuan Wen, Dinesh Jayaraman, and Yang Gao. Can Transformers Capture Spatial Relations between Objects? In *The Twelfth International Conference on Learning Representations*, 2023.
- [59] Dejia Xu, Yifan Jiang, Peihao Wang, Zhiwen Fan, Humphrey Shi, and Zhangyang Wang. SinNeRF: Training Neural Radiance Fields on Complex Scenes from a Single Image. In *European Conference on Computer Vision*, 2022.
- [60] Lihe Yang, Bingyi Kang, Zilong Huang, Xiaogang Xu, Jiashi Feng, and Hengshuang Zhao. Depth Anything: Unleashing the Power of Large-Scale Unlabeled Data. In *Proceedings of the IEEE/CVF Conference on Computer Vision and Pattern Recognition*, pages 10371–10381, June 2024.
- [61] Lihe Yang, Bingyi Kang, Zilong Huang, Zhen Zhao, Xiaogang Xu, Jiashi Feng, and Hengshuang Zhao. Depth Anything V2. *arXiv:2406.09414*, 2024.
- [62] Shukang Yin, Chaoyou Fu, Sirui Zhao, Ke Li, Xing Sun, Tong Xu, and Enhong Chen. A Survey on Multimodal Large Language Models. *arXiv preprint arXiv:2306.13549*, 2024.
- [63] Alex Yu, Vickie Ye, Matthew Tancik, and Angjoo Kanazawa. pixelNeRF: Neural Radiance Fields from One or Few Images. In *Proceedings of the IEEE/CVF Conference on Computer Vision and Pattern Recognition*, 2021.
- [64] Zhen Zeng, Adrian Röfer, and Odest Chadwicke Jenkins. Semantic Linking Maps for Active Visual Object Search (Extended Abstract). In Zhi-Hua Zhou, editor, *Proceedings of the Thirtieth International Joint Conference on Artificial Intelligence, IJCAI-21*, pages 4864–4868. International Joint Conferences on Artificial Intelligence Organization, 8 2021. Sister Conferences Best Papers.
- [65] G. Zhang, Y. Zhang, K. Zhang, and V. Tresp. Can Vision-Language Models be a Good Guesser? Exploring VLMs for Times and Location Reasoning. In *2024 IEEE/CVF Winter Conference on Applications of Computer Vision (WACV)*, pages 625–634, Los Alamitos, CA, USA, jan 2024. IEEE Computer Society.

- [66] Haoyu Zhen, Xiaowen Qiu, Peihao Chen, Jincheng Yang, Xin Yan, Yilun Du, Yining Hong, and Chuang Gan. 3D-VLA: A 3D Vision-Language-Action Generative World Model. In *Proceedings of the 41st International Conference on Machine Learning*, July 2024.
- [67] Tinghui Zhou, Richard Tucker, John Flynn, Graham Fyffe, and Noah Snavely. Stereo Magnification: Learning View Synthesis using Multiplane Images. In *Proceedings of ACM SIGGRAPH*, 2018.
- [68] Yan Zhu, Yuandong Tian, Dimitris Metaxas, and Piotr Dollár. Semantic amodal segmentation. In *IEEE Conference on Computer Vision and Pattern Recognition*, pages 1464–1472, 2017.
- [69] Zhengxia Zou, Keyan Chen, Zhenwei Shi, Yuhong Guo, and Jieping Ye. Object Detection in 20 Years: A Survey. *arXiv preprint arXiv:1905.05055*, 2023.

Appendix

A Additional Scene Processing Details

The COCO objects we considered include the following: refrigerator, TV, bed, chair, sink, oven, book, laptop, couch, and door [27].

Table 3: Scene Information with Target Objects

| Scene No | Scene ID | Timestamp | Objects Not in Image | Scene Category |
|----------|------------------|-----------|----------------------|-----------------------|
| 1 | 2e4013ea92d04301 | 119586133 | Television | Living Room |
| 2 | 2bec33eeeab0bb9d | 34768067 | Sink | Kitchen |
| 3 | 2e64a2d17f9a76f7 | 162629000 | Sink | Kitchen + Dining Room |
| 4 | 2b625e92f2cf9de4 | 51384667 | Refrigerator | Kitchen + Dining Room |
| 5 | 2cb9869cb05a9a01 | 77786042 | Oven | Kitchen + Dining Room |
| 6 | 3c64a373bc1c53bd | 199767000 | Bed | Bedroom |
| 7 | ff6d8ab35e042db5 | 142142000 | Oven | Kitchen + Dining Room |
| 8 | 2bd7cee1fa9c8996 | 51133333 | Chair | Living Room + Study |
| 9 | 3de41ace235a3a13 | 49616000 | Sink | Kitchen + Dining Room |
| 10 | 2d6d5e82bda0611c | 153253000 | Television | Bedroom |

This section outlines supplementary details regarding the scene selection and processing workflow used in this study. Scene Category annotation was automated using a ChatGPT-4o API [36] built in to predict room categories up to three predictions.

Scene Selection Methodology: To ensure even spatial sampling across camera pose sequences, we employed geodesic movement calculations within the special Euclidean group, $\mathcal{SE}(3)$. Since multiple frames may be spatially equidistant in $\mathcal{SE}(3)$, we selected the frame closest in timestamp to each equidistant geodesic point. This approach minimizes redundancy by ensuring that each selected frame captures a unique viewpoint while maintaining a representative spatial distribution. For each scene, we recorded the total pose variation and selected frames that best matched equidistant $\mathcal{SE}(3)$ poses using their timestamps. This ensures consistent spatial sampling across the entire camera movement trajectory. In the absence of meta-labels, we used these images to verify whether the scene is indoor or outdoor using the ChatGPT-4o API [36], and automatically labeled them accordingly for consideration.

Indoor Scene Selection Criteria: We further filtered our selection of indoor scenes using the following criteria:

- *Scene Size:* Scenes with too few images (< 50) were excluded to reduce reconstruction sparsity.
- *Geodesic Movement:* A minimum threshold of spatial movement was imposed to guarantee sufficient variation for 3D representation testing.
- *Object Detection:* Scenes with low COCO object detection rates ($< 60\%$) were automatically filtered out, as they provide lower semantic diversity for the evaluations.

Image Selection from scene: An image is selected if its 360x360 center crop excludes the target object and a unique image from each scene ensures diversity. Additionally, images are not chosen from the first or last 10 timestamps to avoid cross-fading.

Addressing Drift in ORB-SLAM Poses: Since the RealEstate10k dataset employs ORB-SLAM poses, normalized scale extrinsics can drift over long camera trajectories, especially when loop closures are absent [33, 34]. To mitigate this, an epipolar distance-based filter was implemented to remove frames from the temporal edges that showed significant pixel-to-pixel variation between consecutive frames, indicative of potential drift or cross-fading artifacts.

Point Triangulation & Dense Reconstruction: We used *SIFT* to extract up to 50,000 features per image across multiple GPUs, which were then used for sequential matching, followed by point triangulation, which provided us with sufficient matches for dense reconstruction [13].

Post-Reconstruction Filtering: After obtaining the dense reconstruction of the model, we applied point cloud filtering. We followed a basic outlier removal strategy by removing statistical outliers with 10 nearest neighbors and a standard deviation ratio of 0.5.

B Supplementary Information on DFM Sampling & Sample Rejection

In this appendix, we provide detailed information regarding the specific metrics, thresholds, computational considerations, and pose selection process used in our study.

Sample Rejection Metrics: Four key metrics were used for automated sample rejection:

- *Noise Detection:* Noise was quantified using Laplacian variance V_L . Samples with $V_L < \tau_b$ for more than 80% of frames were classified as noisy and discarded. The threshold τ_b was set according to guidelines established in Pertuz et al. [38].
- *Structural Similarity (SSIM):* SSIM was calculated for each frame to assess visual similarity between consecutive frames. Videos where SSIM exceeded τ_s for over 50% of the frames were rejected for showing stagnation or lack of visual variability [56].
- *Pixel Luminosity Variation:* The average pixel intensity L_t was used to track brightness variations across frames. Samples were rejected if changes in luminosity between consecutive frames fell below τ_l for over half the video. This indicates static content or poor lighting conditions.
- *Object Detection Flatness:* Object detection was conducted using Yolov8x [40, 20]. Samples were rejected if no objects were detected with at least 0.5 confidence in 50% or more of the frames at 30 fps.
- *Sparseness Rejection:* We have bounding boxes from the images in the ground truth frame. Scenes were rejected if upon dense stereo-matched reconstruction the obtained point clouds which when the base images (where the object was detected in the ground truth 2D image) was passed through an object detector upon projection did not have at least 100 pixels in the bounding box in every frame.

Computational Limitations: Each run of the DFM model took over 7 days on a single GPU due to the lack of model parallelism support. The model required at least 80GB of VRAM to handle the large number of parameters and data processing [55].

Pose Selection in the $\mathcal{SE}(2)$ Framework: To balance scene diversity and computational efficiency, three target poses were selected for each image. These poses (Pose 1 being the input frame, Figure 2(a)) were chosen based on their ability to cover the scene without blind spots, defined in terms of (x, y, θ) :

- **Pose 2:** $(2, 2, -90^\circ)$ – This pose focused on the eastern (left) boundary of the scene, ensuring coverage of the left and central areas.
- **Pose 3:** $(-2, 2, 90^\circ)$ – This pose complemented Pose 1 by covering the western (right) boundary and central zones.
- **Pose 4:** $(0, 5, 180^\circ)$ – This pose was selected to capture depth and provide a longitudinal perspective from the south.

C Detailed Methodology for VLM Query Process

The following provides additional details on how we implemented VLM query structuring and response processing for the study.

Limiting LLM Hallucination: Large Language Models, despite their visual and language reasoning abilities, cannot entirely prevent hallucinations during token generation [5]. To reduce the likelihood of incorrect outputs, we restricted responses to binary “Yes” or “No” answers. This simplification helped minimize errors caused by the unpredictability of free-form responses, particularly in tasks involving spatial reasoning.

Structured Query Format: We used a standardized query format for all questions, focusing on the presence or relative position of an object in the image. The specific format included queries like:

```
Is it likely that there is a/an [object] to the left of this frame?  
Answer strictly in (Yes/No).  
Is it likely that there is a/an [object] to the right of this frame?  
Answer strictly in (Yes/No).  
Is it likely that there is a/an [object] within the frame of this image?  
Answer strictly in (Yes/No).
```

This strict format ensured that the output was easily interpretable and could be processed further without requiring complex parsing.

Regex and Answer Processing: We employed regular expression (regex) structuring to automate the extraction of “Yes” or “No” answers from the model’s response. The simplicity of binary responses minimized the risk of errors during the answer retrieval process.

Granular Confidence Scoring: For each region (left, right, within the frame), we calculated a granular score based on the fraction of “Yes” answers provided by the model. These scores were then used to create a confidence value for each region-object pair, which formed the basis of the 2D Spatial Semantic Heatmap (SSH). The SSH was treated as a 640×360 heatmap, allowing for easy comparison across models.

Metrics and Heatmap Comparison: The results from the VLM query process were tabulated and compared against other models in the study (Table Table 1), using the generated SSH for both qualitative and quantitative analysis.

Data for Visual Language Models (VLMs) were accessed on September 18, 2024. ChatGPT-4o, Claude-Sonnet-3.5, and Gemini 1.5 Ultra were accessed via official APIs, and QwenVL-Chat and LLaVa-v1.6-34b through the Replicate API: <https://replicate.com/home>. Time limits for token access were adhered to, with wait timers for API access integrated into the pipelines.

D Depth Handling for Experiments

In the 2.5D study with the DFM, we retained points within the camera’s frustum and removed occluded points using a depth buffer. For each pixel, only the 3D point with the smallest depth Z -value was kept to ensure visibility. Frustum culling was then applied to retain points within the near and far clipping planes and the camera’s field of view.

For DFM, operating at room scale, we compared predictions to scale-ambiguous ground truth from COLMAP. Since both operate on the same scale, depths were directly compared.

In DepthAnythingv2, depth estimation defines near and far planes, varying only by a scale factor. Depth values were rescaled uniformly based on the average image depth to maintain consistency. For COLMAP, we projected the reconstructed points onto the image plane and compared depths for valid pixels in both outputs, using global average rescaling to ensure consistency without complex iterative alignment.

In the 3D study, where the grid is sparse and unequal in size between the prediction and ground truth distributions, we pad the grids to match the larger of the two. This ensures comparisons are made over valid domains.

E Standard Deviation Values for the Metrics Presented

In this section, we provide the standard deviation values to the metrics described earlier in Section 4.3 in Table 4, Table 5 and Table 6.

Table 4: Standard deviation values for the 2D task.

| Method vs Metrics | $\mathcal{H}^\times \downarrow$ | $\mathcal{D}^{\text{NN}}(\%) \downarrow$ | $\mathcal{H} \downarrow$ | $\mathcal{A} \uparrow$ |
|-------------------------------|---------------------------------|--|--------------------------|------------------------|
| Uniform Confidence | 0.45 | 0.00 | 0.00 | 0.03 |
| Ground Truth | 0.00 | 0.00 | 0.07 | 0.00 |
| DFM ($n_s = 25, k = 4$) | 0.58 | 0.00 | 0.22 | 0.41 |
| DFM ($n_s = 25, k = 3$) | 0.63 | 0.08 | 0.12 | 0.33 |
| DFM ($n_s = 25, k = 2$) | 0.88 | 0.05 | 0.11 | 0.26 |
| DFM ($n_s = 15, k = 4$) | 0.48 | 0.69 | 0.26 | 0.39 |
| DFM ($n_s = 10, k = 4$) | 0.91 | 1.65 | 0.08 | 0.44 |
| SDXL (with object prompts) | 0.24 | 0.23 | 0.15 | 0.20 |
| SDXL (without object prompts) | 0.39 | 1.32 | 0.08 | 0.23 |
| SDXL (without any prompts) | 0.35 | 0.00 | 0.02 | 0.24 |
| ChatGPT-4 | 0.31 | 0.51 | 0.00 | 0.11 |
| Claude-Sonnet-3.5 | 0.14 | 0.54 | 0.00 | 0.09 |
| Gemini 1.5 Ultra | 0.33 | 0.43 | 0.01 | 0.10 |
| QwenVL-Chat | 0.22 | 0.44 | 0.01 | 0.12 |
| LLaVa-v1.6-34b | 0.21 | 0.17 | 0.01 | 0.18 |

Table 5: Standard deviation values for the 2.5D task

| Method vs Metrics | $\mathcal{H}^\times \downarrow$ | $\mathcal{D}^{\text{NN}}(\%) \downarrow$ | $\mathcal{H} \downarrow$ | $\mathcal{A} \uparrow$ |
|-----------------------------------|---------------------------------|--|--------------------------|------------------------|
| Uniform Confidence | 0.21 | 0.00 | 0.00 | 0.03 |
| Ground Truth | 0.00 | 0.00 | 0.09 | 0.00 |
| DFM ($n_s = 25, k = 4$) | 0.29 | 0.14 | 0.11 | 0.41 |
| DFM ($n_s = 25, k = 3$) | 0.34 | 2.67 | 0.18 | 0.33 |
| DFM ($n_s = 25, k = 2$) | 1.09 | 4.52 | 0.07 | 0.26 |
| DFM ($n_s = 15, k = 4$) | 0.68 | 7.22 | 0.13 | 0.39 |
| DFM ($n_s = 10, k = 4$) | 1.72 | 5.08 | 0.17 | 0.44 |
| SDXL + DAv2 (with object prompts) | 0.14 | 6.13 | 0.17 | 0.20 |
| SDXL + DAv2 (without cues) | 0.39 | 4.52 | 0.14 | 0.23 |
| SDXL + DAv2 (without prompts) | 5.13 | 0.00 | 0.06 | 0.24 |

Table 6: Standard deviation values for the 3D task

| Method | $\mathcal{H}^\times \downarrow$ | $\mathcal{D}^{\text{NN}}(\%) \downarrow$ | $\mathcal{H} \downarrow$ |
|---------------------------|---------------------------------|--|--------------------------|
| Uniform Confidence | 0.49 | 0.00 | 0.00 |
| Expanded Context Frustum | 0.52 | 0.20 | 0.36 |
| DFM ($n_s = 25, k = 4$) | 0.26 | 0.09 | 0.09 |
| DFM ($n_s = 25, k = 3$) | 0.92 | 1.11 | 0.08 |
| DFM ($n_s = 25, k = 2$) | 2.75 | 7.34 | 0.19 |
| DFM ($n_s = 15, k = 4$) | 1.48 | 1.16 | 0.17 |
| DFM ($n_s = 10, k = 4$) | 4.75 | 5.77 | 0.15 |